

# Assessing the spatiotemporal variation in anthropogenic heat and its impact on the surface thermal environment over global land areas

Kai Jin<sup>a,b</sup>, Fei Wang<sup>b,c,d</sup>, Shaoxia Wang<sup>a,\*</sup>

<sup>a</sup> Qingdao Engineering Research Center for Rural Environment, College of Resources and Environment, Qingdao Agricultural University, Qingdao 266109, China

<sup>b</sup> Institute of Soil and Water Conservation, Northwest A&F University, Yangling 712100, China

<sup>c</sup> Institute of Soil and Water Conservation, Chinese Academy of Sciences and Ministry of Water Resources, Yangling 712100, China

<sup>d</sup> University of Chinese Academy of Sciences, Beijing 100049, China



## ARTICLE INFO

### Keywords:

Anthropogenic heat  
Land surface  
thermal  
environment  
Solar radiation  
Temperature  
City

## ABSTRACT

Anthropogenic heat that is mainly released in cities is rapidly rising in the context of global warming, while its impact on the land surface thermal environment is not completely clear. This study compared the anthropogenic heat flux (AHF) with the surface net solar radiation (SNSR) and analyzed the relationship between AHF and the surface urban heat island effect ( $E_{SUHI}$ ) on the basis of the estimation and analysis of global terrestrial AHF. Results indicated that the global-averaged terrestrial AHF caused by energy consumption and human metabolism increased from 0.07 to 0.15 W/m<sup>2</sup> from 1980 to 2018. While a decrease in AHF mainly occurred in the developed cities of Europe and the United States, developing cities, particularly in eastern China, experienced an increase in AHF. The averaged terrestrial AHFs were far less than the corresponding SNSRs at the global and continental scales, whereas they were generally comparable in urban areas. AHF in the 100 largest cities around the globe was 19.56 (6.54) W/m<sup>2</sup> in 2018 (1980) on average, which was approximately 12% (4%) of the corresponding SNSR. Additionally, we found a significantly positive correlation between AHF and  $E_{SUHI}$  in eastern China ( $R^2 = 0.8383$ ,  $P < 0.01$ ). These findings imply that anthropogenic heat has a considerable impact on the land surface thermal environment and is one of the most important contributors to dramatic urban warming, which needs to be considered in future climate-related policy formulation and evaluation.

## 1. Introduction

Anthropogenic heat refers to the heat released to the atmosphere as a result of human activity, often involving the combustion of fuels and human metabolism (Lee, Song, Baik, & Park, 2009; Sailor, 2011). Anthropogenic heat can substantially affect evapotranspiration (Cong, Shen, Zhou, Sun, & Liu, 2017), wind speed (Zhang, Wang, Chen, Dai, & Wang, 2016), temperature (Flanner, 2009), and precipitation (Feng, Wang, & Yan, 2014) by changing the land surface energy balance and disrupting the normal atmospheric circulation pattern from local to global scales. In urban areas, anthropogenic heat release is generally more severe than that in rural areas and often leads to dramatic warming (He, Zhou, Yao, Ma, & Kinney, 2020; Kato & Yamaguchi, 2005; Wang, Hu, Chen, & Yu, 2019; He, Zhou et al., 2020). As a result, the health of residents and environment in cities has been affected by local anthropogenic heat release (Patz, Campbell-Lendrum, Holloway, & Foley, 2005). Analyzing the AHF variation and its impacts on the land surface

thermal environment and energy balance, particularly for urban areas, plays an important role in not only understanding the impact of human activity on climate but also facilitating environmental management.

Anthropogenic heat flux (AHF) was generally used to represent the intensity of anthropogenic heat release (Jin, Wang, Chen et al., 2019). Previous studies have generally been focused on the estimation of AHF magnitude (Gabey, Grimmond, & Capel-Timms, 2019) and show that AHF has increased on average from 0.03 to 0.10 W/m<sup>2</sup> from 1965 to 2013 over global lands (Lu et al., 2017). While global energy consumption and population size have rapidly increased over the past few decades, they show a large spatial divergence owing to economic, cultural, and historical differences among the different countries (Azad, Rasul, Khan, Sharma, & Bhuiya, 2015; Hamza & Gilroy, 2011; Linard, Gilbert, Snow, Noor, & Tatem, 2012; Wang et al., 2018). With the development of the world economy and technologies, energy consumption is expected to continually change in the future (Lu et al., 2017). Consequently, anthropogenic heat release often shows large

\* Corresponding author.

E-mail address: [wang-sx@hotmail.com](mailto:wang-sx@hotmail.com) (S. Wang).

spatiotemporal heterogeneity. Some globally gridded AHF datasets with different spatial resolutions and temporal ranges have been proposed in the past decade (Allen, Lindberg, & Grimmond, 2010; Flanner, 2009; Yang et al., 2017). However, most of the AHF datasets cover a relatively short period and have a relatively rough spatial resolution, with which the demands of research at the local scale are difficult to meet. Based on a top-down inventory-based approach, Jin, Wang, Chen et al. (2019) recently developed a new global AHF dataset with fine spatial resolution (30 arc-second) and a long-term time series (1970–2050). Their AHF dataset was demonstrated to be relatively accurate by multiple validations; however, they did not consider heat from human metabolism, which was relatively high in cities. To better evaluate the impacts of anthropogenic heat on the land surface thermal environment and energy balance, especially in urban areas, it is necessary to consider both energy consumption and human metabolism for AHF estimation.

Existing studies of climatic impacts of anthropogenic heat have been typically conducted based on the numerical simulation of climate models, which provide quantified results (Chen, Dong et al., 2016; Chen, Yang, & Wu, 2016). For example, using the integrated Weather Research and Forecasting (WRF)/Urban Modeling system, Chen, Dong et al. (2016); Chen, Yang et al. (2016) suggested that the mean UHI intensity reached 0.95 °C in winter in Hangzhou City, China, and anthropogenic heat contributed 65.26% to UHI intensity. Based on the WRF model, Feng et al. (2014) suggested that the increase in the regional average surface air temperature due to anthropogenic heat release reached 0.6–1.0 °C in three vast urban areas in China. Moreover, based on a global climate model, Zhang, Cai, and Hu (2013) demonstrated that the inclusion of energy use at 86 model grid points where it exceeds 0.4 W/m<sup>2</sup> can lead to an increase of as much as 1 K in surface temperature during winter and autumn in the mid- and high latitudes of North America and Eurasia. However, the inner relationship between anthropogenic heat release and land surface thermal environment was difficult to extract according to these quantified results, which hindered understanding of its impact mechanisms.

According to the law of conservation of energy, solar energy received by the land surface could be converted into other forms of energy rather than disappearing (Wang et al., 2017). In natural lands, the surface net radiation (SNR) is the total energy received by the land surface and is equal to the sum of the soil heat flux, sensible heat flux, and latent heat flux (Han, Ma, Chen, & Su, 2017). SNR is also equal to the sum of surface net solar radiation (SNSR) and surface net thermal radiation (SNTR) fluxes (Li, Yang, Tang, Sun, & Fang, 2011). SNSR and SNTR represent the gain and loss of energy in land surface, respectively (Dutton, 1990). For urban lands, a large amount of anthropogenic heat can be converted into sensible and latent heat fluxes, resulting in local warming (Park, Schade, Werner, Sailor, & Kim, 2016). The AHF in some large cities even exceeded SNSR and SNR. For example, the annual mean AHF during the daytime exceeded 400 W/m<sup>2</sup> for some grids of 250 m × 250 m in central Tokyo, Japan, and the maximum AHF of a grid reached 1590 W/m<sup>2</sup> in winter (Ichinose, Shimodozo, & Hanaki, 1999). Therefore, SNSR, SNTR, and AHF were often treated as inputs to the land surface energy balance equation in previous studies on the estimation of AHF in urban areas (Offerle, Grimmond, & Fortuniak, 2005; Sailor, 2011). Several studies have focused on the impacts of anthropogenic heat on the land surface energy balance in particular cities (e.g., Hangzhou, China and São Paulo, Brazil) by comparative analysis and suggested that the ratios of AHF to SNSR (AHF/SNSR) ranged from 10% to 20% (Ferreira, Oliveira, & Soares, 2011; Jin, Wang, Liu, Gou, & Ding, 2019). However, the divergence in the impact of anthropogenic heat on the land surface energy balance among different cities of the entire planet is not entirely clear.

In this study, we aimed to explore the impact of anthropogenic heat on the land surface thermal environment by comparing AHF with SNSR and analyzing the relationship between AHF and land surface temperature (LST) with an emphasis on cities. Before this, the spatiotemporal variation in AHF during 1980–2018 was investigated based on

population size, population density, and energy consumption data. This study could enhance our knowledge of the impact of anthropogenic heat on climate warming and the sustainable development of social and environment.

## 2. Materials and Methods

### 2.1. Data Collection

Global gridded population density data in 1980 and 2015 with a spatial resolution of 30 arc-seconds were downloaded from the Socio-economic Data and Applications Center (SEDAC) in the Earth Observing System Data and Information System (EOSDIS) of National Aeronautics and Space Administration (NASA) (<http://sedac.ciesin.columbia.edu/data/sets/browse>). The annual total population data of the world by region and country for 1980–2018 were obtained from World Population Prospects 2019, which was downloaded from the Department of Economic and Social Affairs of the United Nations (<https://population.un.org/wpp/Download/Standard/Population/>). The abovementioned population data were used to calculate AHF due to human metabolism and serve as a proxy of the redistribution of the total energy consumption.

The annual primary energy consumption data during 1980–2018 used in this study were obtained from the British Petroleum Statistical Review of World Energy (BP Review) (<https://www.bp.com/>). The primary energy in the BP Review comprised commercially traded fuels, including modern renewables used to generate electricity, and their statistics were taken from government sources and published data. Early versions of the BP Review have been frequently used for the study of AHF (Jin, Wang, Chen et al., 2019; Lu et al., 2017). The entire world was classified into seven sub-regions by the BP Review in 2018, comprising 92 countries and regions. Because of the variations and complications of historical country boundaries, in this study, two sub-regions (i.e., Europe and Commonwealth of Independent States) were merged into one sub-region based on a previous version of the BP Review. The final six global sub-regions included Africa (AF), Asia Pacific (AP), Europe and Eurasia (EE), Middle East (ME), North America (NA), and South and Central America (SCA) (Fig. 1). This study used energy statistics from the latest BP Review to estimate the magnitude of AHF caused by energy consumption at the global, continental, city, and grid scales.

The monthly SNSR data with a spatial resolution of 7.5 arc-minutes for 1980–2018 were obtained from the ERA-Interim reanalysis dataset of the European Centre for Medium-Range Weather Forecasts (<http://apps.ecmwf.int/datasets/>). The ERA-Interim reanalysis dataset included many types of climatic elements (e.g., temperature, precipitation, solar radiation) and was produced by using a sequential data assimilation scheme and forecast model. Compared with its previous generation (i.e., ERA-40), there was substantial improvement in the ERA-Interim reanalysis data, such as improved representation of the hydrological cycle, more realistic stratospheric circulation, and better temporal consistency on a range of timescales. Because of the high spatial resolution (up to 7.5 arc-minutes) and long time span (1979–2019), ERA-Interim reanalysis data have been widely used in climate change research (Tang et al., 2019).

Monthly mean LST data during daytime and nighttime from 2015 were obtained from Geospatial Data Cloud site, Computer Network Information Center, Chinese Academy of Sciences (<http://www.gscloud.cn>). The LST data with a resolution of 1 km were composited from the MODIS/Aqua products and were used to represent the land surface thermal environment in eastern China. The annual mean LST in 2015 was calculated by averaging the monthly mean LSTs during daytime and nighttime. Additionally, the land use dataset of China from 2015 at 1 km resolution was provided by the Data Centre for Resources and Environmental Sciences, Chinese Academy of Sciences (<http://www.resdc.cn/Default.aspx>). The land use dataset was used to identify urban and non-urban areas in eastern China.

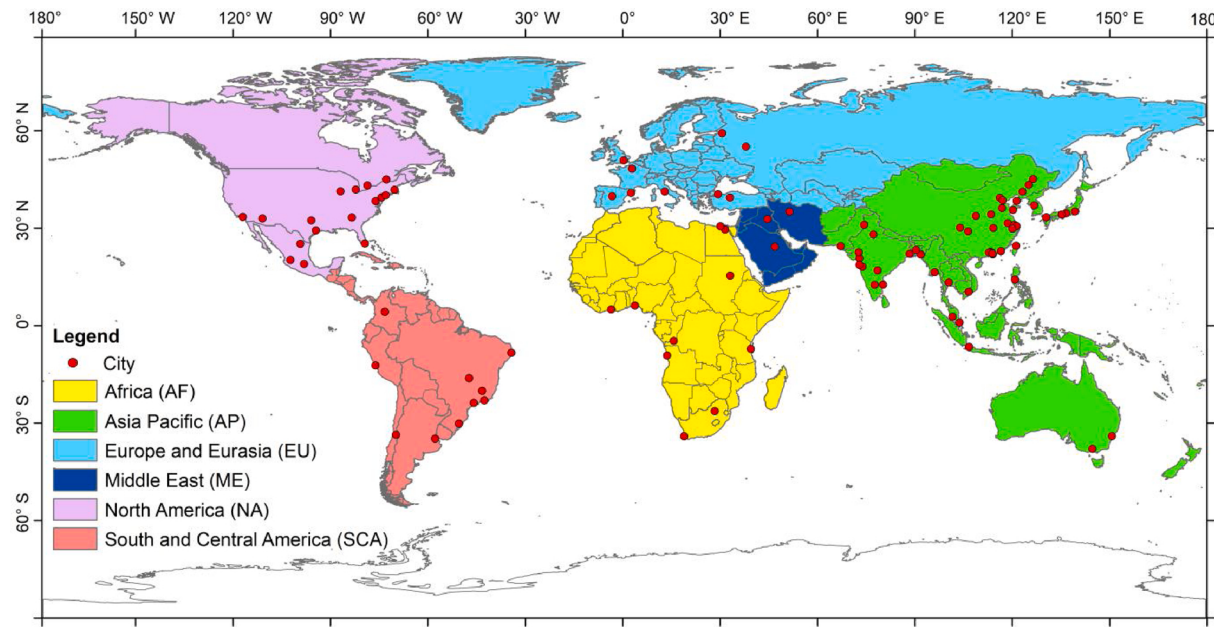


**Fig. 1.** Locations of the six sub-regions and the selected 100 largest cities in the world.

The 100 largest cities in the world ranked by population size in 2010 were selected (Fig. 1). The Global Man-Made Impervious Surface (GMIS) dataset for 2010 from Landsat was used to determine urban areas for the selected cities, which were obtained from the SEDAC in the EOSDIS of NASA (<http://sedac.ciesin.columbia.edu/data/sets/browse>). The spatial resolution of the GMIS data was 1 km, and its pixel values ranged from 0% to 100%. The pixel values of GMIS data show the percentage of impervious surfaces, such as buildings, roads, parking lots, and other man-made surfaces (Brown de Colstoun et al., 2019). The percentage of impervious surfaces is a key indicator in assessing the urban environment and has been widely used to explore the degree of urbanization (Song, Sexton, Huang, Channan, & Townshend, 2016). In the study of Voorde, Jacquet, and Canters (2011), while spatial entities with 10% or less impervious surface cover were assigned to the class of non-urban land, the entities with an impervious surface cover more than 10% were classified into six urban land-use types. Therefore, based on the GMIS dataset, we identified and extracted urban areas where the values of the pixels were larger than 10% for the selected 100 largest cities. Additionally, country land areas were downloaded from the World Bank Open Data (<https://data.worldbank.org/>), which were used to calculate the total terrestrial areas for the seven sub-regions and the entire world. The areas under inland water bodies (e.g., major rivers and lakes) were excluded in the country land areas.

## 2.2. Methods

### 2.2.1. Estimation of regional averaged terrestrial AHF

Because of the difficulties in observing and estimating the fuel-to-heat conversion efficiency, we assumed that all the consumed energy was eventually converted into heat, and the delay between energy use and its realization as heat was ignored (Chen, Dong, Shi, Li, & Chen, 2014; Lu et al., 2017; Pigeon, Legain, Durand, & Masson, 2007). Thus, the averaged terrestrial AHF due to energy consumption and human metabolism in the six sub-regions and the entire world from 1980–2018 could be calculated according to Eq. (1)–(3) (Dong, Varquez, & Kanda, 2017).

$$AHF = AHF_e + AHF_m \quad (1)$$

$$AHF_e = \frac{E_{total}}{S \times t} \times c \text{ and} \quad (2)$$

$$AHF_m = \frac{P_{total} \times (Q_1 \times t_1 + Q_2 \times t_2)}{S \times (t_1 + t_2)} = \rho \times Q_m \quad (3)$$

where  $AHF_e$  and  $AHF_m$  indicate the average anthropogenic heat fluxes induced by energy consumption and human metabolism in a given region, respectively, in  $\text{W/m}^2$ ;  $E_{total}$  indicates the annual total energy consumption in a given region in tonne oil equivalent (toe);  $S$  represents the total terrestrial area in  $\text{m}^2$ ;  $t$  is the total time of a given year in s;  $c$  is the energy conversion coefficient,  $1 \text{ toe} = 42 \times 10^9 \text{ J}$ ;  $P_{total}$  refers to the total population in a given region;  $Q_1$  and  $Q_2$  indicate the daytime and nocturnal metabolic rates, respectively; and  $t_1$  and  $t_2$  represent the daytime and nocturnal lengths in one day, respectively. Based on Sailor and Lu (2004),  $Q_1$  and  $Q_2$  are set as 175 and 75 W, respectively,  $t_1$  and  $t_2$  are set to be 16 and 8 h, respectively,  $\rho$  indicates the average population density in a region per  $\text{m}^2$ ; and  $Q_m$  indicates the average human metabolic rate in one day (i.e., 141.7 W) (Jin, Wang, Liu et al., 2019).

### 2.2.2. Estimation of global gridded AHF

Global gridded AHFs in 1980 and 2018 were calculated by summing over the heat released from energy consumption and human metabolism for each pixel. The heat released from human metabolism for each pixel was calculated based on Eq. 3 and the gridded population density. The global population density in 2018 was estimated by multiplying the population density of each country (region) in 2015 by the corresponding population growth ratio (ratio of the population size in 2018 to that in 2015). Based on the study of Jin, Wang, Chen et al. (2019), the total energy consumption in each country (region) was apportioned using the population density and total population size and then converted to the annual mean gridded energy flux (Eq. 4). This method was generally correct except for few regions, such as some suburban areas that house relatively few people or energy-hungry industries (Jin, Wang, Chen et al., 2019; Lu, Wang, Zhang, Sun, & Qian, 2016).

$$AHF_e = \frac{E_{total} \times \frac{P_{grid}}{P_{total}}}{S_{grid} \times t} \times c = \frac{E_{total} \times c}{P_{total} \times t} \times \rho_{grid} \quad (4)$$

where  $P_{grid}$  refers to the population represented by each pixel in a given region;  $S_{grid}$  represents the pixel area in  $\text{m}^2$ ; and  $\rho_{grid}$  refers to the gridded population density in a given region per  $\text{m}^2$ , which is equal to the ratio of  $P_{grid}$  to  $S_{grid}$ .

### 2.2.3. Analysis of AHF variation and its impact on land surface thermal environment

Based on the estimation of AHF, spatiotemporal changes in the annual mean terrestrial AHF from 1980–2018 were explored at the global, continental, and city scales; the maximum and average AHFs for each selected city were calculated. The mean annual SNSRs during 1980–2018 were used to calculate the average SNSRs for the selected 100 cities, six sub-regions, and entire planet. It is difficult to evaluate the impact of anthropogenic heat on the land surface energy balance with real spatial measurements (Wang et al., 2017). For urban areas, both AHF and SNSR are the gain of energy of land surface, whereas SNLR is the loss of energy from land surface (Dutton, 1990). Therefore, we compared the magnitudes and trends between AHF and SNSR at different spatial scales. AHF/SNSR was calculated based on the regionally averaged AHF and SNSR. The trend rates of AHF and SNSR were calculated using ordinary least-squares regression. This study takes eastern China as an example to explore the relationship between anthropogenic heat intensity and LST. The total land was initially divided into regular latitude-longitude grid boxes ( $50\text{ km} \times 50\text{ km}$ ). Then, the surface urban heat island effect ( $E_{\text{SUHI}}$ ) was calculated for each grid box by subtracting the average annual mean LST of the pixels located in non-urban areas from the average annual mean LST of all pixels in 2015. Based on the land use dataset in eastern China, the regions excluding construction lands were identified as non-urban areas, in which the LSTs were assumed to be nearly free from AHF impacts. Because of the cloud impact, some pixels in the LST images had no value. Therefore, a given grid box was excluded if the area of the pixels containing LST values accounted for less than 50% of the total area of the grid box. Ultimately, 214 grid boxes were selected to calculate  $E_{\text{SUHI}}$ . Linear regression analysis was undertaken between the mean AHF and  $E_{\text{SUHI}}$  to explain their relationship. In this study, calculations based on raster data were conducted by ArcGIS 10.2 software, and Antarctica, as well as inland water areas, were ignored.

## 3. Results

### 3.1. Spatio-temporal variation of global AHF

The averaged global terrestrial AHF caused by energy consumption and human metabolism increased from  $0.07$  to  $0.15\text{ W/m}^2$  from 1980 to 2018 (Fig. 2). Moreover, the six sub-regions of the world showed a great difference in the change in the averaged terrestrial AHF during 1980–2018 (Fig. 2). Among the six sub-regions, NA and EE displayed larger AHF before 2000, whereas AP and ME exhibited larger AHF after 2010. While the AHF of NA experienced a relatively rapid increase before 2000, it showed an invisible trend with some fluctuations after 2000. The AHF of EE slowly increased before 1990 and fluctuations decreased from 1990 to 2018. Additionally, increases in AHF from AP

and ME were more rapid than those from NA and EE in the study period. In contrast, SCA and AF exhibited a relatively slow increase in AHF during the study period. Overall, the averaged terrestrial AHFs of AF, AP, EE, ME, NA, and SCA were estimated to be  $0.03$  ( $0.01$ ),  $0.29$  ( $0.04$ ),  $0.15$  ( $0.11$ ),  $0.23$  ( $0.02$ ),  $0.19$  ( $0.12$ ), and  $0.06$  ( $0.01$ )  $\text{W/m}^2$  in 2018 (1980), respectively.

Areas with an AHF ranging from  $0.01$  to  $0.1\text{ W/m}^2$  in 1980 were mainly located in southern and eastern Asia, southwestern Russia, northern and southern Europe, eastern US, Central America, eastern Brazil, and part of Africa (Fig. 3a). The areas with an AHF ranging from  $0.1$  to  $0.5\text{ W/m}^2$  in 1980 were fewer and mainly located in central and eastern Europe, eastern US, northeastern India, and eastern China. There were only a few pixels with AHF higher than  $1.0\text{ W/m}^2$  in 1980, which were sporadically distributed in developed areas, such as the large cities of US, Europe, and Japan. In 2018, areas with AHF ranging from  $0.01$  to  $0.10\text{ W/m}^2$  were significantly enlarged in Africa, South America, and ME relative to 1980 (Fig. 3b). There were large areas for which the AHFs increased up to above  $1.0\text{ W/m}^2$  in 2018 in South and East Asia (e.g., China, India, and Japan). Notably, the sites with AHF greater than  $2.00\text{ W/m}^2$  were extended from having a spotted distribution to being continuously distributed from 1980 to 2018 in eastern China. Overall, AHFs in many cities located in the middle latitudes of the Northern Hemisphere were larger than those in the Southern Hemisphere over the past decades. During 1980–2018, while southern and eastern Asia experienced rapid increase in AHF, some developed regions of Europe and United States showed a decrease in AHF (Fig. 3c). Moreover, many areas in ME also showed a relatively rapid increase in AHF during the study period.

Fig. 4 shows that the mean AHFs in 1980 and 2018 are extremely different among the selected 100 cities in the world. While the mean AHFs of the selected 100 cities varied from  $0.28\text{ W/m}^2$  (Luanda) to  $47.61\text{ W/m}^2$  (New York) in 1980, they varied from  $0.73\text{ W/m}^2$  (Khartoum) to  $285.23\text{ W/m}^2$  (Singapore) in 2018 (see Table S1 in the e-Component). Whereas 69 cities showed a mean AHF smaller than  $5\text{ W/m}^2$  in 1980, 10 cities showed a mean AHF larger than  $20\text{ W/m}^2$  (Fig. 4a). In contrast, there were 29 cities with a mean AHF larger than  $20\text{ W/m}^2$  in 2018, which were mainly located in Europe, eastern United States, and southeastern Asia (Fig. 4b). The number of cities with a mean AHF smaller than  $5\text{ W/m}^2$  in 2018 was smaller than that in 1980, and the cities were mainly located in Africa and Southwest Asia. On average, the mean AHFs of the selected 100 cities were  $6.54$  and  $19.56\text{ W/m}^2$  in 1980 and 2018, respectively. Moreover, there were 36 cities that showed a maximum AHF that was larger than the corresponding mean SNSR in 2018, indicating that their maximum AHFs were comparable to the corresponding mean SNSRs (Table S1).

### 3.2. Comparisons between AHF and SNSR

In the period 1980–2018, whereas the trends in AHF of the six global sub-regions varied from  $0$  to  $0.06\text{ W/m}^2/\text{decade}$ , the trends in SNSR of the six global sub-regions varied from  $-0.33$  to  $0.78\text{ W/m}^2/\text{decade}$  (Table 1). The trend in global-averaged terrestrial SNSR from 1980 to 2018 was  $0.33\text{ W/m}^2/\text{decade}$ , which was extremely small compared with the magnitude of the annual mean SNSR (approximately  $134\text{ W/m}^2$  in global lands). The trend in global-averaged terrestrial AHF ( $0.02\text{ W/m}^2/\text{decade}$ ) was approximately  $1/16$  of that for SNSR. Moreover, the trend in AHF for ME ( $0.05\text{ W/m}^2/\text{decade}$ ) was approximately  $1/7$  of that for SNSR. AP exhibited an AHF trend of  $0.06\text{ W/m}^2/\text{decade}$ , whereas the corresponding trend for SNSR was  $-0.33\text{ W/m}^2/\text{decade}$ . The AHF/SNSR ratio of the six global sub-regions varied from  $0$  (AF) to  $0.17\%$  (EE) in 1980 (Table 1). Except for EE, the other five sub-regions showed increases in AHF/SNSR in 2018 compared with that in 1980. Among the six sub-regions, NA and EE showed the largest AHF/SNSR in 2018 (i.e.,  $0.17\%$ ). AHF/SNSR of the world in 1980 and 2018 was estimated to be  $0.05\%$  and  $0.11\%$ , respectively. Overall, at the global and continent scales, the magnitudes of averaged terrestrial AHF were far less than that

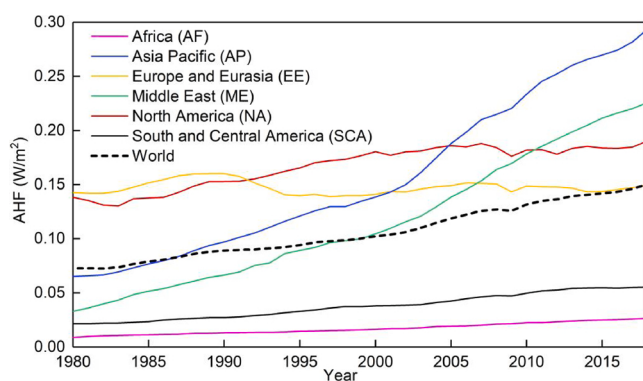


**Fig. 2.** Temporal change of averaged terrestrial anthropogenic heat flux (AHF) for the entire planet and six sub-regions from 1980 to 2018.

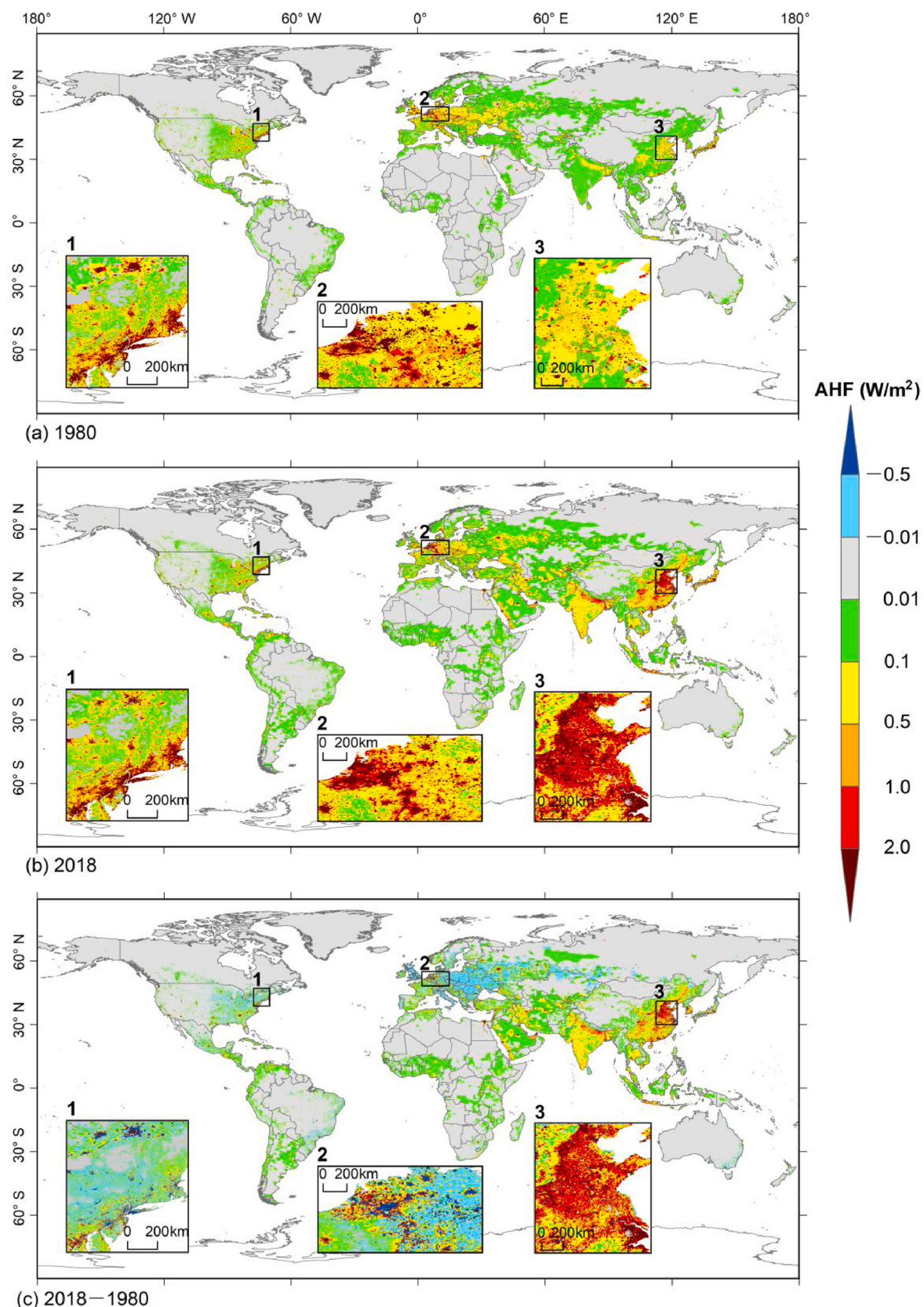


**Fig. 3.** Spatial distribution of anthropogenic heat flux (AHF) in (a) 1980 and (b) 2018 and (c) the difference in AHF between 1980 and 2018 over the entire planet.

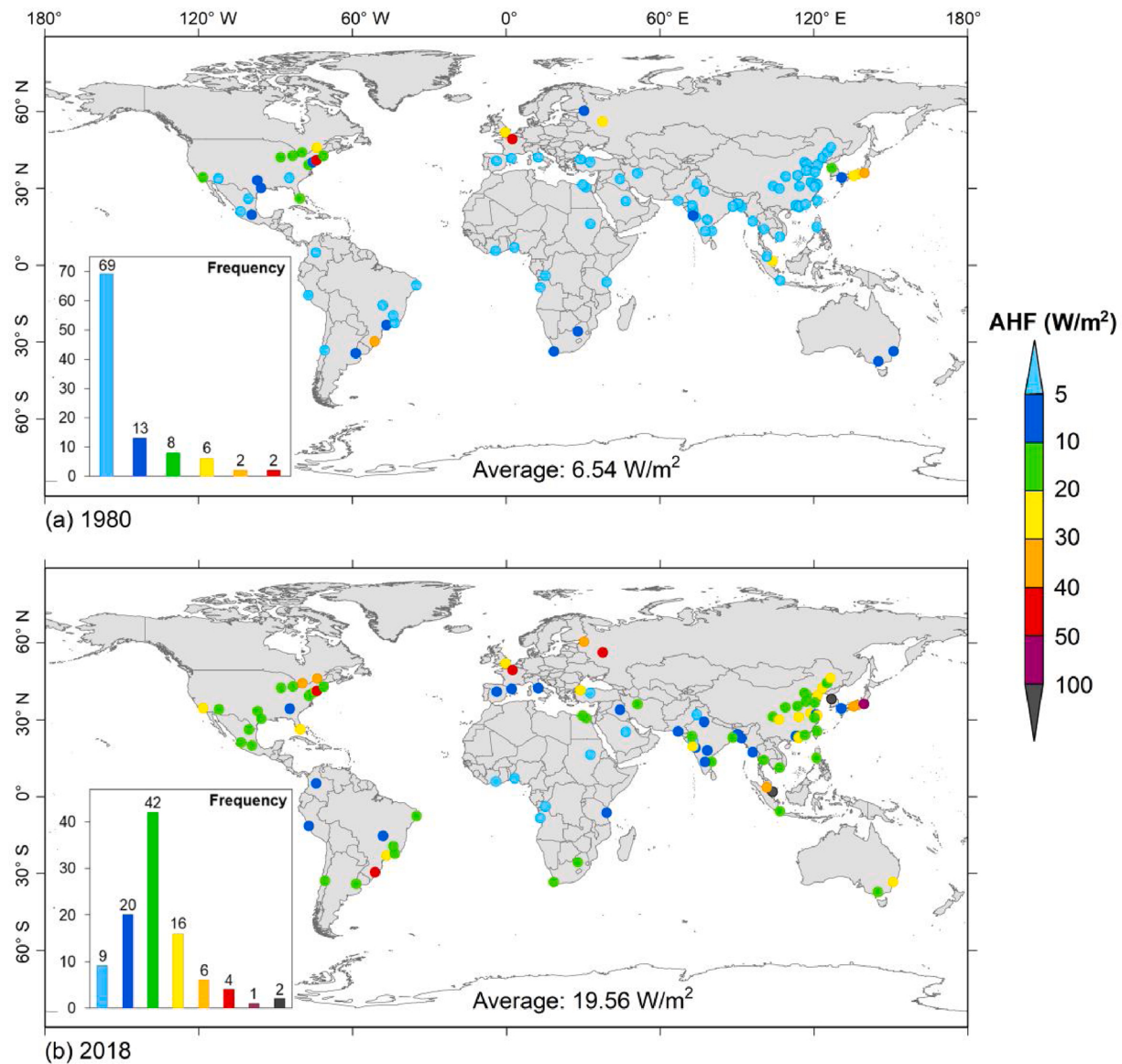


**Fig. 4.** Spatial distribution of the mean anthropogenic heat flux (AHF) in the selected 100 largest cities of the world in (a) 1980 and (b) 2018.

**Table 1**

Trends of the averaged terrestrial anthropogenic heat flux (AHF) and surface net solar radiation (SNSR) from 1980 to 2018 and the ratios of AHF to SNSR (AHF/SNSR) in 1980 and 2018 over the entire planet and six sub-regions.

Region	Trend rate (W/m <sup>2</sup> /decade)		AHF/SNSR (%)	
	AHF	SNSR	1980	2018
AF	0	0.78	0	0.01
AP	0.06	-0.33	0.04	0.18
EE	0	0.48	0.17	0.17
ME	0.05	0.34	0.02	0.12
NA	0.02	0.44	0.12	0.17
SCA	0.01	-0.01	0.01	0.03
Entire planet	0.02	0.33	0.05	0.11

Note: AF, AP, EE, ME, NA, and SCA represent Africa, Asia Pacific, Europe and Eurasia, Middle East, North America, and South and Central America, respectively. Antarctica and inland water areas are not considered in the calculations.

of SNSR in the study period, and their long-term trends were more than one order of magnitude lower than that of SNSR except for SCA.

The mean annual SNSRs during 1980–2018 generally ranged from 50 W/m<sup>2</sup> to 230 W/m<sup>2</sup> in the six global sub-regions (see Fig. S1 in the e-

Component). While SNSRs in the low-latitude regions were generally larger than those in the high-latitude regions, SNSRs near the equator were generally lower than those in the regions near 30°N and 30°S. Fig. 5 shows that most lands around the globe exhibit an extremely small AHF/SNSR (lower than 0.01%) in 1980 and 2018. The areas with relatively large AHF/SNSR (higher than 0.1%) were mainly located in eastern US, Europe, and eastern Asia in 1980 (Fig. 5a). The areas with relatively large AHF/SNSR were enlarged in 2018 relative to 1980, especially in eastern China (Fig. 5b). For those metropolitan regions of the world, such as the urban areas of the northeastern United States and central Europe, AHF/SNSR of pixels in 1980 and 2018 were generally higher than 5.0%. Moreover, urban areas with an AHF/SNSR higher than 5.0% in 2018 significantly increased in eastern China compared with that in 1980.

Whereas 58 cities showed an AHF/SNSR lower than 2% in 1980, 13 cities showed an AHF/SNSR higher than 10% and were mainly located in Japan, northeastern United States, and Europe (Fig. 6a). There were 36 cities with an AHF/SNSR higher than 10% in 2018, which were triple in number relative to that in 1980 (Fig. 6b). The cities with an AHF/SNSR higher than 10% in 2018 relative to 1980 were mainly located in AP. There were 13 cities with an AHF/SNSR higher than 20% in 2018,

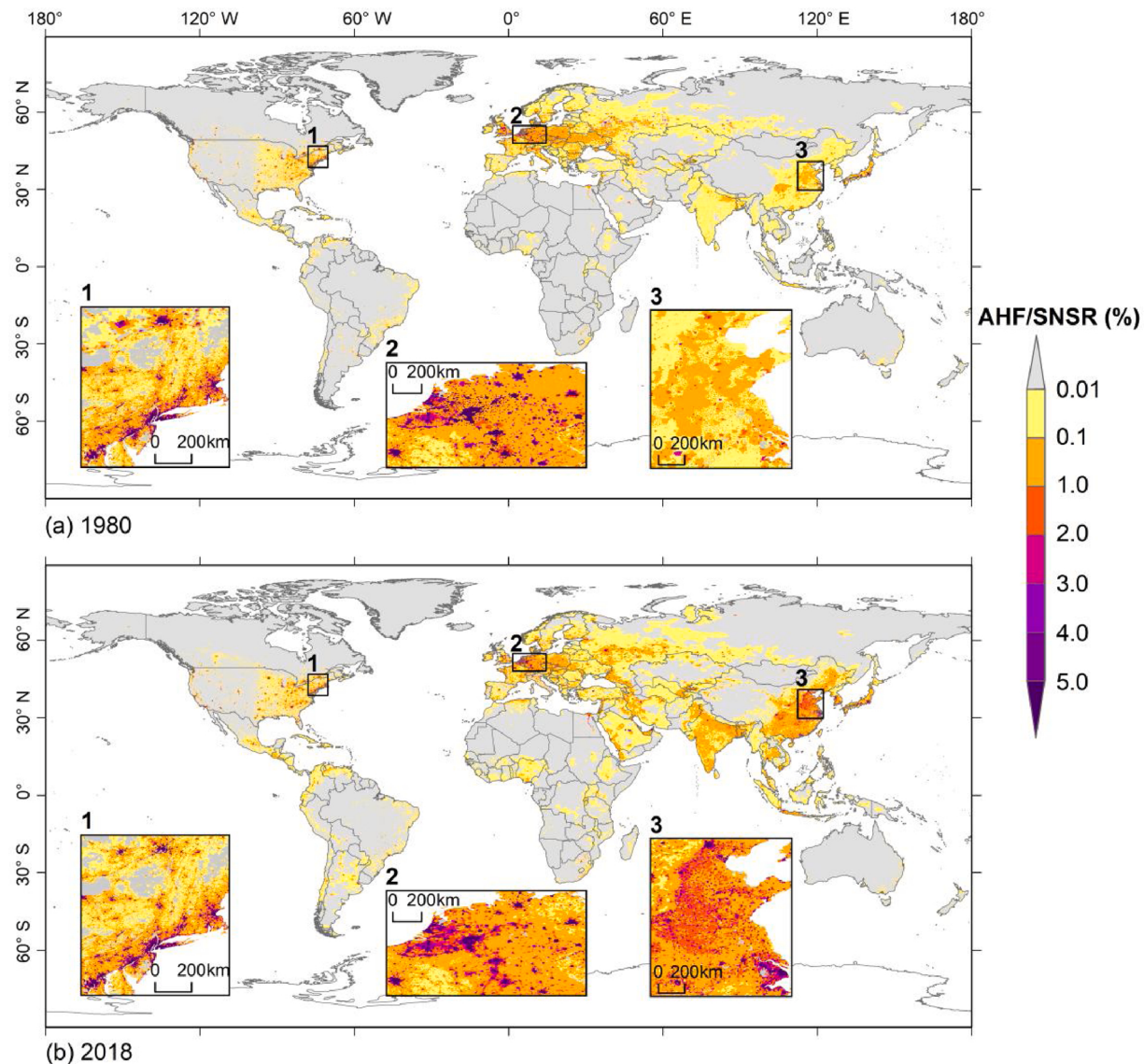


**Fig. 5.** Spatial distribution of the ratios of anthropogenic heat flux to surface net solar radiation (AHF/SNSR) in (a) 1980 and (b) 2018 over the entire planet.

which were mainly located north of 30°N. Moreover, the highest AHF/SNSRs of the selected 100 cities were estimated to be 30% (Paris) and 143% (Singapore) in 1980 and 2018, respectively (Table S1). The average AHF/SNSR of the selected 100 cities was approximately 12% in 2018, triple that of 1980.

### 3.3. Relationship between AHF and LST

Eastern China has experienced rapid urbanization since the 1980s with a dramatic growth in AHF. Construction lands generally showed an AHF larger than 8 W/m<sup>2</sup> in eastern China in 2015 (Fig. 7a and b). LSTs in urban areas were generally higher than those in the surrounding non-urban areas; such areas are considered as surface urban heat islands (Fig. 7a and 7c). We further calculated the average EsUHI for each of the selected 214 grids in 2015 (Fig. 7d). The distribution of EsUHI was consistent with that of AHF. The grids with relatively high EsUHI were mainly located in large cities that are economically developed and densely populated. For example, grids located in the cities of Beijing, Tianjin, Jinan, and Shanghai showed an annual mean EsUHI higher than 0.1 °C.

The largest EsUHI of the grid box of 50 km × 50 km reached 0.87 °C (Fig. 8). Based on the data of the selected 214 grids located in eastern

China, we found a significant positive correlation between AHF and EsUHI ( $R^2 = 0.8383$ ,  $P < 0.01$ ), indicating that EsUHI was closely associated with the change in AHF at the grid scale (Fig. 8). The regression equation between AHF and EsUHI was  $y = 0.0275x - 0.0179$ , which implied that LST would increase by 0.0275 °C for each 1.0 W/m<sup>2</sup> increase in AHF in the context of urbanization. Moreover, for the grids with AHF between 0 and 8 W/m<sup>2</sup>, the positive correlation between AHF and EsUHI was also significant at the 0.01 significance level. Considering the rapid increase in AHF during 1980–2018 in the selected 100 largest cities, EsUHI may be dramatically enlarged, especially for the cities located in SCA and AP.

## 4. Discussion

This study found that the averaged global terrestrial AHF caused by energy consumption and human metabolism reached 0.15 W/m<sup>2</sup> in 2018, which was higher than the results of Dong et al. (2017) and Lu et al. (2017). The averaged global terrestrial AHFs were estimated to be 0.13 and 0.10 W/m<sup>2</sup> in 2013 by Dong et al. (2017) and Lu et al. (2017), respectively. Difference in the estimation was partly attributed to the increase in energy consumption recently. Moreover, this study and Dong et al. (2017) estimated AHF by considering energy consumption and

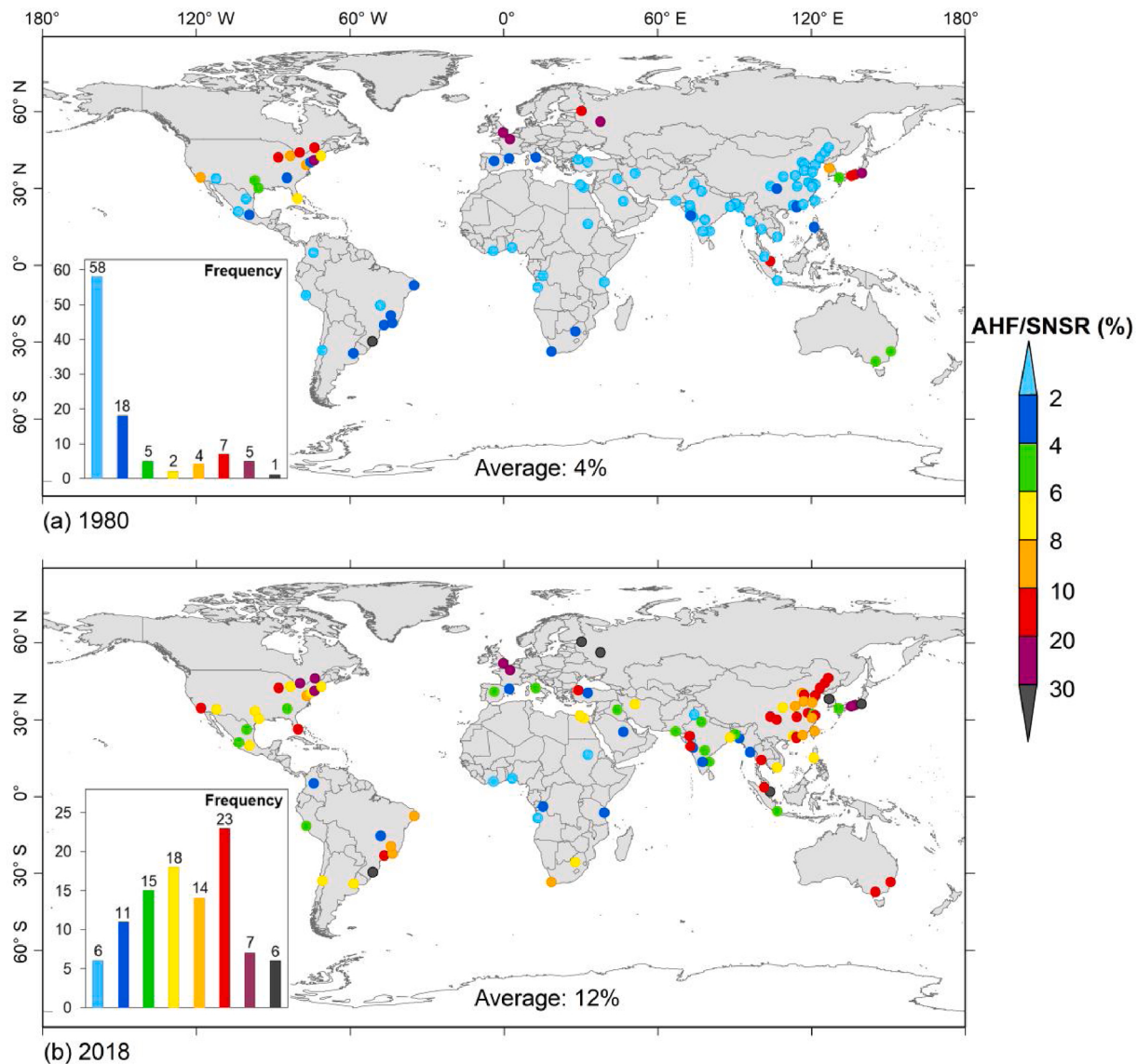


**Fig. 6.** Spatial distribution of the ratios of mean anthropogenic heat flux to mean surface net solar radiation (AHF/SNSR) in the selected 100 largest cities of the world in (a) 1980 and (b) 2018.

human metabolism, whereas Lu et al. (2017) ignored the heat released from human metabolism.

We found that the changes in AHF were extremely uneven over the world during 1980–2018. Whereas developing cities experienced rapid increase in AHF during the study period, some developed regions such as large cities located in the northeastern United States, showed a decrease in AHF (Fig. 3c). With the robust growth of the global economy in recent decades, the economic and energy structures of many countries have experienced changes of varying degrees. The weakening of AHF in some developed regions was closely related to the decline in energy consumption by the shifting economic structure (Mukherjee, 2008a), changing energy consumption type (Cuce & Riffat, 2016), and improving energy use efficiency (Hamza & Gilroy, 2011). However, the impacts of the changes in the economic and energy consumption structures on energy consumption intensity were marginal in developing countries (e.g., China and India) (Feng, Sun, & Zhang, 2009; Mukherjee, 2008b). Consequently, developing regions generally showed a rapid increase in AHF during 1980–2018.

While the magnitudes of the averaged terrestrial AHF were far less than those of SNSR at the global and continental scales, their long-term trends were comparable to a certain extent (Table 1). Moreover, AHFs

were comparable to the radiative forcing caused by other anthropogenic activities at large scales. For example, the mean radiative forcing due to the albedo variation associated with the change in land cover from 1990 to 2010 was  $0.062 \text{ W/m}^2$  in China (Zhai, Liu, Liu, Zhao, & Huang, 2014), which was lower than the increase in AHF in AP (i.e.,  $0.14 \text{ W/m}^2$ ) during the same period. Moreover, Zhang and Caldeira (2015) demonstrated that the energy released from the combustion of fossil fuels was approximately 1.71% of the radiative forcing from  $\text{CO}_2$  that has accumulated in the atmosphere as a consequence of historical fossil fuel combustion. The emissions of accumulated  $\text{CO}_2$  from 1750 to 2011 have resulted in a radiative forcing of  $1.68$  ( $1.33\text{--}2.03$ )  $\text{W/m}^2$  (IPCC, 2013). Therefore, the global-averaged terrestrial AHF in 2018 (i.e.,  $0.15 \text{ W/m}^2$ ) was approximately 9% of the radiative forcing of accumulated  $\text{CO}_2$  since the industrial revolution. The impacts of anthropogenic heat on the land surface energy balance have led to large-scale climate change (Flanner, 2009). Chen et al. demonstrated that the anthropogenic heat release could disturb atmospheric circulation, resulting in an increase of  $0.02$  ( $0.10$ ) K for the global mean surface temperature in boreal summer (winter) (Chen, Dong et al., 2016; Chen, Yang et al., 2016). With the increase in economic development, radiative forcing induced by energy consumption was predicted to continually increase in future decades

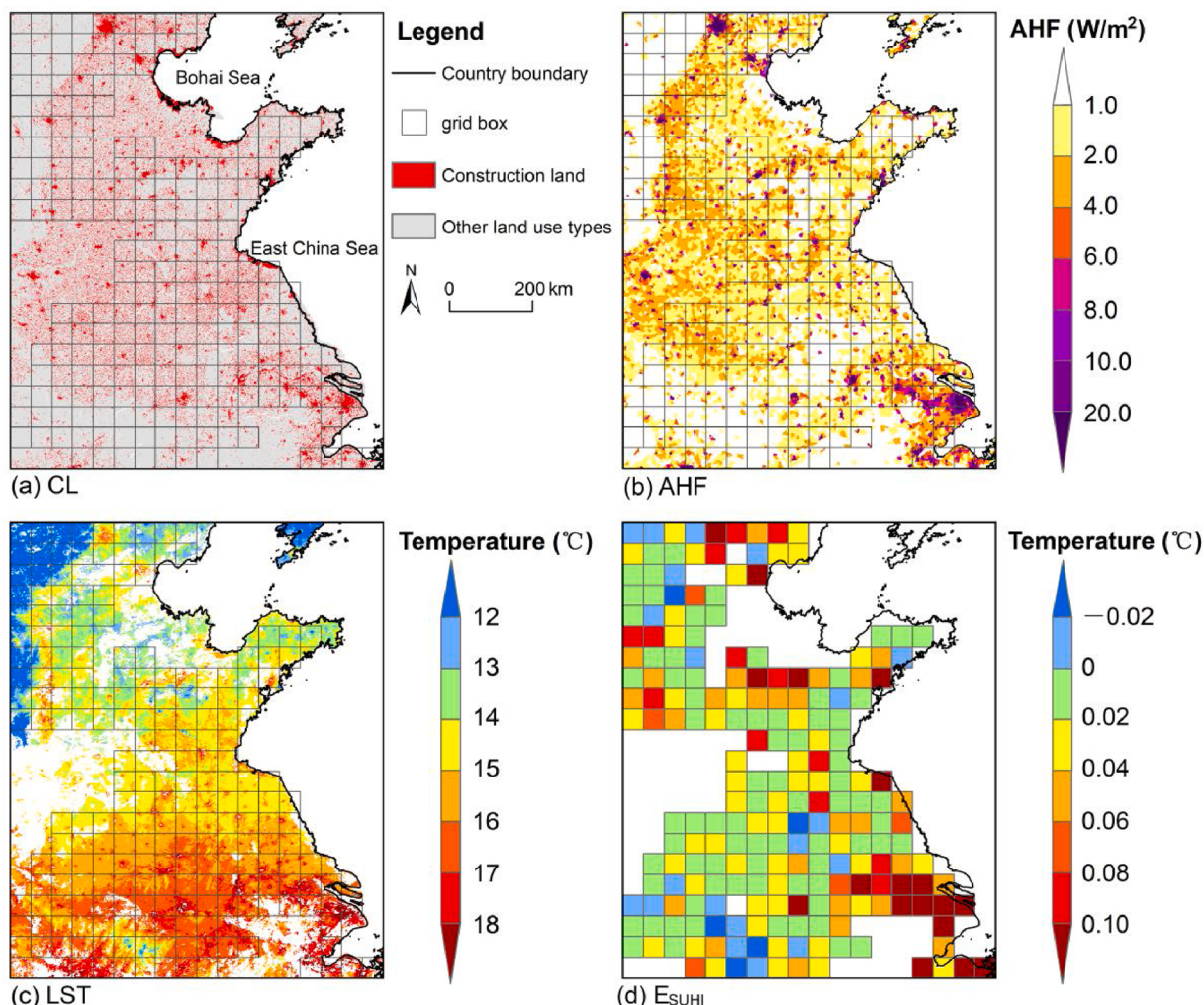


**Fig. 7.** Spatial distribution of (a) construction land, (b) anthropogenic heat flux, (c) land surface temperature, and (d) surface urban heat island effect over eastern China in 2015.

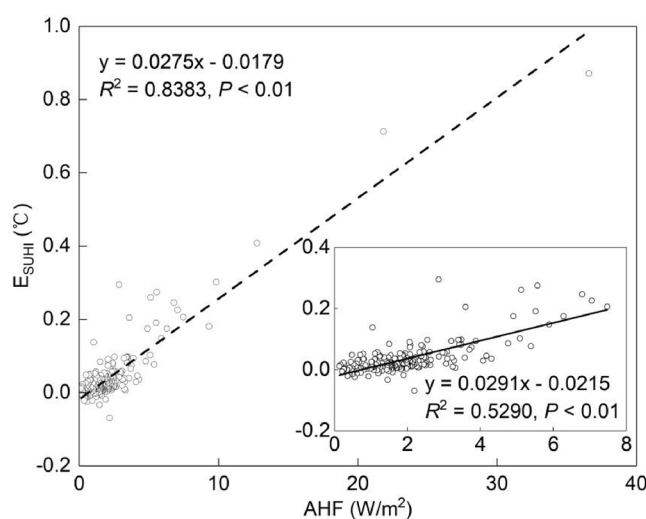


**Fig. 8.** The relationship between anthropogenic heat flux (AHF) and surface urban heat island effect (EsUHI) for the selected 214 grids of  $50 \text{ km} \times 50 \text{ km}$  in eastern China.

(Jin, Wang, Chen et al., 2019). Therefore, we suggest that more attention should be paid to the climatic forcing of the anthropogenic heat release when researching large-scale climate changes.

The city is the most concentrated area of energy consumption and human activity. Among the 100 largest cities of the world, there were 29 cities with a mean AHF larger than  $20 \text{ W/m}^2$  and 36 cities with a maximum AHF larger than the corresponding SNSRs in 2018 (Table S1). Lu et al. (2016) reported that AHFs in eastern China were mostly between 0.5 and  $20 \text{ W/m}^2$  in 2010. Whereas AHF in London (UK) was estimated to be  $26.2 \text{ W/m}^2$  in 2015 (Allen et al., 2010), it reached  $87.5 \text{ W/m}^2$  in Seoul, Republic of Korea in 2000 (Lee et al., 2009). The above-mentioned results indicate that the intensity of anthropogenic heat release is much higher at the city scale than that at the regional and global scales. Moreover, Ferreira et al. demonstrated that the annual mean AHFs were near 11% of the SNSR from 2004 to 2007 in São Paulo, Brazil (Ferreira et al., 2011). The averaged AHF/SNSR of the 31 provincial capital cities of China was approximately 12% in 2015 (Jin, Wang, Liu et al., 2019). These results are consistent with those of the current study, implying a great influence of anthropogenic heat on land surface energy balance in urban areas.

As an important input of energy in the urban canopy, the AHF in cities could largely affect local and regional changes in climate (Murray & Heggie, 2016). This study found a significantly positive correlation between AHF and EsUHI at the grid scale ( $R^2 = 0.8383$ ,  $P < 0.01$ ), and LST was expected to increase by  $0.0275^\circ\text{C}$  for each  $1.0 \text{ W/m}^2$  increase in

AHF in the context of urbanization. The warming in the cities was generally caused by both anthropogenic heat and the impacts of construction land (e.g., enhancing solar radiation absorbance and sensible heat conversion) (Tysa et al., 2016; Sun, Wang, & Wang, 2020). Therefore, the above-mentioned result does not mean that an AHF increase of  $1.0 \text{ W/m}^2$  would necessarily lead to a warming of  $0.0275^\circ\text{C}$ ; rather, it highlights the important role of AHF in urban warming. Moreover, the abovementioned result was based on eastern China only and may not be the case for every country/continent. At regional scale, AHFs in the areas located in the middle latitudes of the Northern Hemisphere were larger than those in the Southern Hemisphere over the past few decades (Fig. 5). This is related to the massive numbers of residents and vast energy consumption in cities (Allen et al., 2010; Peng et al., 2012) and may be one of the reasons for the significant warming occurring over the mid- and high latitudes in the Northern Hemisphere (Zhang et al., 2013). Therefore, the impact of anthropogenic heat release should not be ignored in the city planning for environmental health and socioeconomic development.

This study estimated AHF based on population and energy consumption data and the potential assumption that energy consumption is linearly correlated with population size. This assumption is generally correct except for few regions, such as some suburban areas that house relatively few people or large industries (Jin, Wang, Chen et al., 2019; Lu et al., 2016). Moreover, the daily commute of urban population can alter the spatiotemporal pattern of energy consumption (Yang, Hu, & Wang, 2019), which was not considered in this study. We qualitatively assessed the impact of anthropogenic heat release on the land surface thermal environment. However, the intensity of anthropogenic heat release is often associated with regional background climate conditions (Lindberg, Grimmond, Yugeswaran, Kotthaus, & Allen, 2013; Wang & Wang, 2017), implying a potential variation of its impacts on the land surface thermal environment at different seasons and regions. For example, during the Northern Hemisphere winter months, apart from the energy consumption for normal production, a massive amount of energy is consumed for residential heating because of the cold climate; during the Northern Hemisphere summer months, the relatively high AHF is mainly caused by the use of cooling systems (Moriwaki, Kanda, Senoo, Hagishima, & Kinouchi, 2008). Generally, the higher the summer temperature is, the more anthropogenic heat that is released from the utilization of the cooling systems and the higher the outdoor air temperature. It's a vicious circle which has a strong negative impact on the sustainability of cities. Therefore, the impact of anthropogenic heat release on the land surface thermal environment throughout the year as well as its quantitative analysis should be given further study in the future.

## 5. Conclusions

In this study, the spatiotemporal variation of the annual mean AHF induced by energy consumption and human metabolism over the entire planet was detected based on energy and population data. On this basis, the impacts of anthropogenic heat release on the land surface thermal environment, particularly for urban areas, were assessed by comparing AHF with SNSR and relating AHF to LST. The main results are as follows.

- (1) Global-averaged terrestrial AHF increased from  $0.07$  to  $0.15 \text{ W/m}^2$  from 1980 to 2018. The spatiotemporal variations in global AHF during the study period showed dramatic heterogeneity. Pixels with high AHF were mainly located in metropolitan regions where a large amount of energy was consumed and massive numbers of people lived. While a decrease in AHF mainly occurred in the developed regions of Europe and United States, developing regions such as eastern China were the main beneficiaries of an increase in AHF. Overall, the averaged terrestrial AHFs of AF, AP, EE, ME, NA, and SCA were estimated to be  $0.03$

- (0.01),  $0.29$  ( $0.04$ ),  $0.15$  ( $0.11$ ),  $0.23$  ( $0.02$ ),  $0.19$  ( $0.12$ ), and  $0.06$  ( $0.01$ )  $\text{W/m}^2$  in 2018 (1980), respectively.
- (2) Global terrestrial AHF/SNSR ratios were estimated to be  $0.05\%$  and  $0.11\%$  in 1980 and 2018, respectively. Among the six sub-regions of the world, EE showed the largest AHF/SNSR in 1980 (i.e.,  $0.17\%$ ), whereas AP showed the largest AHF/SNSR in 2018 (i.e.,  $0.18\%$ ). Although the averaged terrestrial AHFs were far less than SNSRs at global and continental scales, their long-term trends during 1980–2018 were comparable. The pixels in metropolitan regions generally showed an AHF/SNSR higher than  $5.0\%$ .
- (3) Whereas the mean AHFs of the selected 100 largest cities in the world varied from  $0.28 \text{ W/m}^2$  (Luanda) to  $47.61 \text{ W/m}^2$  (New York) in 1980, they varied from  $0.73 \text{ W/m}^2$  (Khartoum) to  $285.23 \text{ W/m}^2$  (Singapore) in 2018. On average, the mean AHFs in the selected 100 cities were  $6.54$  and  $19.56 \text{ W/m}^2$  in 1980 and 2018, respectively. Consequently, the average AHF/SNSR of these cities was approximately  $12\%$  in 2018, tripled that from 1980. Among the selected 100 cities, there were 13 cities with an AHF/SNSR higher than  $20\%$  in 2018, which were mainly located north of  $30^\circ\text{N}$ ; the maximum AHF was larger than the corresponding SNSR in 36 cities.
- (4) In eastern China, the distribution of areas with relatively high LST was consistent with that of areas with relatively high AHF; there was a significantly positive correlation between AHF and Esuhi ( $R^2 = 0.8383$ ,  $P < 0.01$ ). Anthropogenic heat release has greatly affected urban land surface thermal environment, leading to a  $0.0275^\circ\text{C}$  warming for each  $1.0 \text{ W/m}^2$  increase in AHF associated with the impact of urbanization.

Because severe anthropogenic heat release contributes to the dramatic warming in urban areas, more energy has to be consumed for cooling systems in hot season; then, higher outdoor air temperature may be induced. This vicious circle tends to harm health of people and add social and environmental external costs in cities. Therefore, we suggest that climatic forcing of anthropogenic heat should be paid more attention not only in the use of simulations in urban, regional, and global climate research but also in policy formulation for combating climate change and facilitating socioeconomic sustainability.

## Declaration of Competing Interest

The authors report no declarations of interest.

## Acknowledgements

This study was supported by the Foundation of High-level Talents of Qingdao Agricultural University [Grant number 663/1120104, 665/1120041] and the National Nature Science Foundation of China [Grant number 41771558].

## Appendix A. Supplementary data

Supplementary material related to this article can be found, in the online version, at doi:<https://doi.org/10.1016/j.scs.2020.102488>.

## References

- Allen, L., Lindberg, F., & Grimmond, C. S. B. (2010). Global to city scale urban anthropogenic heat flux: model and variability. *Int. J. Climatol.*, 31, 1990–2005. <https://doi.org/10.1002/joc.2210>.
- Azad, A. K., Rasul, M. G., Khan, M. M. K., Sharma, S. C., & Bhuiya, M. M. K. (2015). Study on Australian energy policy, socio-economic, and environment issues. *J. Renewable Sustainable Energy*, 7, Article 063131. <https://doi.org/10.1063/1.4938227>.
- Brown de Colstoun, E. C., Huang, C., Wang, P., Tilton, J. C., Tan, B., Phillips, J., et al. (2019). Global Man-made Impervious Surface (GMIS) Dataset From Landsat. *NASA Socioeconomic Data and Applications Center (SEDAC)*. Available online: <https://doi.org/10.7927/H4P55KKF> (accessed on October 1, 2019).

- Chen, B., Dong, L., Liu, X., Shi, G. Y., Chen, L., Nakajima, T., et al. (2016). Exploring the possible effect of anthropogenic heat release due to global energy consumption upon global climate: a climate model study. *Int. J. Climatol.*, 36, 4790–4796. <https://doi.org/10.1002/joc.4669>.
- Chen, B., Dong, L., Shi, G., Li, L. J., & Chen, L. F. (2014). Anthropogenic heat release: estimation of global distribution and possible climate effect. *J. Meteorolog. Soc. Jpn.*, 92A, 157–165. <https://doi.org/10.2151/jmsj.2014-A10>.
- Chen, F., Yang, X., & Wu, J. (2016). Simulation of the urban climate in a Chinese megacity with spatially heterogeneous anthropogenic heat data. *J. Geophys. Res. Atmos.*, 121, 5193–5212. <https://doi.org/10.1002/2015JD024642>.
- Cong, Z. T., Shen, Q. N., Zhou, L., Sun, T., & Liu, J. H. (2017). Evapotranspiration estimation considering anthropogenic heat based on remote sensing in urban area. *Sci. China Earth Sci.*, 60, 659–671. <https://doi.org/10.1007/s11430-016-0216-3>.
- Cuce, E., & Riffat, S. B. (2016). A comprehensive assessment of sectoral energy consumption in the UK: past, present and future. *Int. J. Low-Carbon Technol.*, 11, 424–430. <https://doi.org/10.1093/ijlct/ctv013>.
- Dutton, E. G. (1990). Annual Forcing of the Surface Radiation Balance Diurnal Cycle Measured from a High Tower near Boulder. *Colorado. J. Clim.*, 3, 1400–1408.
- Dong, Y., Varquez, A. C. G., & Kanda, M. (2017). Global anthropogenic heat flux database with high spatial resolution. *Atmos. Environ.*, 150, 276–294. <https://doi.org/10.1016/j.atmosenv.2016.11.040>.
- Feng, J., Wang, J., & Yan, Z. (2014). Impact of anthropogenic heat release on regional climate in three vast urban agglomerations in China. *Adv. Atmos. Sci.*, 31, 363–373. <https://doi.org/10.1007/s00376-013-3041-z>.
- Feng, T., Sun, L., & Zhang, Y. (2009). The relationship between energy consumption structure, economic structure and energy intensity in China. *Energy Policy*, 37, 5475–5483. <https://doi.org/10.1016/j.enpol.2009.08.008>.
- Ferreira, M. J., Oliveira, A. P., & Soares, J. (2011). Anthropogenic heat in the city of São Paulo, Brazil. *Theor. Appl. Climatol.*, 104, 43–56. <https://doi.org/10.1007/s00704-010-0322-7>.
- Flanner, M. G. (2009). Integrating anthropogenic heat flux with global climate models. *Geophys. Res. Lett.*, 36, Article L02801. <https://doi.org/10.1029/2008GL036465>.
- Gabey, A. M., Grimmond, C. S. B., & Capel-Timms, I. (2019). Anthropogenic heat flux: advisable spatial resolutions when input data are scarce. *Theor. Appl. Climatol.*, 135, 791–807. <https://doi.org/10.1007/s00704-018-2367-y>.
- Hamza, N., & Gilroy, R. (2011). The challenge to UK energy policy: an ageing population perspective on energy saving measures and consumption. *Energy Policy*, 39, 782–789. <https://doi.org/10.1016/j.enpol.2010.10.052>.
- Han, C., Ma, Y., Chen, X., & Su, Z. (2017). Trends of land surface heat fluxes on the Tibetan Plateau from 2001 to 2012. *Int. J. Climatol.*, (37), 4757–4767. <https://doi.org/10.1002/joc.5119>.
- He, C., Zhou, L., Yao, Y., Ma, W., & Kinney, P. L. (2020). Estimating spatial effects of anthropogenic heat emissions upon the urban thermal environment in an urban agglomeration area in East China. *Sustainable Cities and Society*, 57, Article 102046. <https://doi.org/10.1016/j.scs.2020.102046>.
- Ichinose, T., Shimodzonoo, K., & Hanaki, K. (1999). Impact of anthropogenic heat on urban climate in Tokyo. *Atmos. Environ.*, 33, 3897–3909. [https://doi.org/10.1016/s1352-2310\(99\)00132-6](https://doi.org/10.1016/s1352-2310(99)00132-6).
- IPCC, et al. (2013). Summary for Policymakers. In T. F. Stocker, D. Qin, G. K. Plattner, M. Tignor, S. K. Allen, & J. Boschung (Eds.), *Climate Change 2013: The Physical Science Basis. Contribution of Working Group I to the Fifth Assessment Report of the Intergovernmental Panel on Climate Change*. Cambridge, United Kingdom and New York, NY, USA: Cambridge University Press.
- Jin, K., Wang, F., Chen, D., Liu, H., Ding, W., & Shi, S. (2019). A new global gridded anthropogenic heat flux dataset with high spatial resolution and long-term time series. *Sct. Data*, 6, 139. <https://doi.org/10.1038/s41597-019-0143-1>.
- Jin, K., Wang, F., Liu, H., Gou, J., & Ding, W. (2019). Spatio-temporal changes of anthropogenic heat release and its impact on land surface energy balance over China. *China Environ. Sci.*, 39, 980–987 (in Chinese) <http://www.zghjkx.com.cn/CN/Y2019/V39/I3/980>.
- Kato, S., & Yamaguchi, Y. (2005). Analysis of urban heat-island effect using ASTER and ETM+ Data: Separation of anthropogenic heat discharge and natural heat radiation from sensible heat flux. *Remote Sens. Environ.*, 99, 44–54. <https://doi.org/10.1016/j.rse.2005.04.026>.
- Lee, S. H., Song, C. K., Baik, J. J., & Park, S. U. (2009). Estimation of anthropogenic heat emission in the Gyeonggi-Region of Korea. *Theor. Appl. Climatol.*, 96, 291–303. <https://doi.org/10.1007/s00704-008-0040-6>.
- Li, X., Yang, X., Tang, J., Sun, X., & Fang, J. (2011). Multiple Urban heat islands and surface energy balance during summer in Yangtze River Delta city cluster region simulated with WRF/NCAR. *J. Meteorol. Sci.*, 31, 441–450 (in Chinese).
- Linard, C., Gilbert, M., Snow, R. W., Noor, A. M., & Tatem, A. J. (2012). Population Distribution, Settlement Patterns and Accessibility across Africa in 2010. *PLoS ONE*, 7, Article e31743. <https://doi.org/10.1371/journal.pone.0031743>.
- Lindberg, F., Grimmond, C. S. B., Yogeswaran, N., Kotthaus, S., & Allen, L. (2013). Impact of city changes and weather on anthropogenic heat flux in Europe 1995–2015. *Urban Clim.*, 4, 1–15. <https://doi.org/10.1016/j.ulclim.2013.03.002>.
- Lu, Y., Wang, H., Wang, Q., Zhang, Y., Yu, Y., & Qian, Y. (2017). Global anthropogenic heat emissions from energy consumption, 1965–2100. *Clim. Change*, 145, 459–468. <https://doi.org/10.1007/s10584-017-2092-z>.
- Lu, Y., Wang, Q., Zhang, Y., Sun, P., & Qian, Y. (2016). An estimate of anthropogenic heat emissions in China. *Int. J. Climatol.*, 36, 1134–1142. <https://doi.org/10.1002/joc.4407>.
- Moriwaki, R., Kanda, M., Senoo, H., Hagishima, A., & Kinouchi, T. (2008). Anthropogenic water vapor emissions in Tokyo. *Water Resour. Res.*, 44, Article W11424. <https://doi.org/10.1029/2007WR006624>.
- Mukherjee, K. (2008a). Energy use efficiency in U.S. manufacturing: A nonparametric analysis. *Energy Econ.*, 30, 76–96. <https://doi.org/10.1016/j.eneco.2006.11.004>.
- Mukherjee, K. (2008b). Energy use efficiency in the Indian manufacturing sector: An interstate analysis. *Energy Policy*, 36, 662–672. <https://doi.org/10.1016/j.enpol.2007.10.015>.
- Murray, J., & Heggie, D. (2016). From urban to national heat island: The effect of anthropogenic heat output on climate change in high population industrial countries. *Earth's Future*, 4, 298–304. <https://doi.org/10.1002/2016EF000352>.
- Offerle, B., Grimmond, C. S. B., & Fortuniak, K. (2005). Heat storage and anthropogenic heat flux in relation to the energy balance of a central European city centre. *Int. J. Climatol.*, 25, 1405–1419. <https://doi.org/10.1002/joc.1198>.
- Park, C., Schade, G. W., Werner, N. D., Sailor, D. J., & Kim, C. H. (2016). Comparative estimates of anthropogenic heat emission in relation to surface energy balance of a subtropical urban neighborhood. *Atmos. Environ.*, 126, 182–191. <https://doi.org/10.1016/j.atmosenv.2015.11.038>.
- Patz, J. A., Campbell-Lendrum, D., Holloway, T., & Foley, J. A. (2005). Impact of regional climate change on human health. *Nature*, 438, 310–317. <https://doi.org/10.1038/nature04188>.
- Peng, S., Piao, S., Ciais, P., Friedlingstein, P., Ottle, C., Bréon, F. M., et al. (2012). Surface urban heat island across 419 global big cities. *Environ. Sci. Technol.*, 46, 696–703. <https://doi.org/10.1021/es2030438>.
- Pigeon, G., Legain, D., Durand, P., & Masson, V. (2007). Anthropogenic heat release in an old European agglomeration (Toulouse, France). *Int. J. Climatol.*, 27, 1969–1981. <https://doi.org/10.1002/joc.1530>.
- Sailor, D. J. (2011). A review of methods for estimating anthropogenic heat and moisture emissions in the urban environment. *Int. J. Climatol.*, 31, 189–199. <https://doi.org/10.1002/joc.2106>.
- Sailor, D. J., & Lu, L. (2004). A top-down methodology for developing diurnal and seasonal anthropogenic heating profiles for urban areas. *Atmos. Environ.*, 38, 2737–2748. <https://doi.org/10.1016/j.atmosenv.2004.01.034>.
- Song, X. P., Sexton, J. O., Huang, C., Channan, S., & Townsend, J. R. (2016). Characterizing the magnitude, timing and duration of urban growth from time series of Landsat-based estimates of impervious cover. *Remote Sens. Environ.*, 175, 1–13. <https://doi.org/10.1016/j.rse.2015.12.027>.
- Sun, Y., Wang, S., & Wang, Y. (2020). Estimating local-scale urban heat island intensity using nighttime light satellite imageries. *Sustainable Cities and Society*, 57, Article 102125. <https://doi.org/10.1016/j.scs.2020.102125>.
- Tang, C., Morel, B., Wild, M., Pohl, B., Abiodun, B., & Bessafi, M. (2019). Numerical simulation of surface solar radiation over Southern Africa. Part 1: Evaluation of regional and global climate models. *Clim. Dynam.*, 52, 457–477. <https://doi.org/10.1007/s00382-018-4143-1>.
- Tysa, S. K., Ren, G., Qin, Y., Zhang, P., Ren, Y., Jia, W., et al. (2016). Urbanization effect in regional temperature series based on a remote sensing classification scheme of stations. *J. Geophys. Res. Atmos.*, 124, 10646–10661. <https://doi.org/10.1029/2019JD030948>.
- Voorde, T. V. D., Jacquet, W., & Canters, F. (2011). Mapping form and function in urban areas: an approach based on urban metrics and continuous impervious surface data. *Landscape Urban Plann.*, 102, 143–155. <https://doi.org/10.1016/j.landurbplan.2011.03.017>.
- Wang, C. H., & Wang, Z. H. (2017). Projecting population growth as a dynamic measure of regional urban warming. *Sustainable Cities and Society*, 32, 357–365. <https://doi.org/10.1016/j.scs.2017.04.010>.
- Wang, L., Wang, S., Zhou, Y., Liu, W., Hou, Y., Zhu, J., et al. (2018). Mapping population density in China between 1990 and 2010 using remote sensing. *Remote Sens. Environ.*, 210, 269–281. <https://doi.org/10.1016/j.rse.2018.03.007>.
- Wang, S., Hu, D., Chen, S., & Yu, C. (2019). A partition modeling for anthropogenic heat flux mapping in China. *Remote Sens.*, 11, 1132. <https://doi.org/10.3390/rs11091132>.
- Wang, X., Guo, W., Qiu, B., Liu, Y., Sun, J., & Ding, A. (2017). Quantifying the contribution of land use change to surface temperature in the lower reaches of the Yangtze River. *Atmos. Chem. Phys.*, 17, 4989–4996. <https://doi.org/10.5194/acp-17-4989-2017>.
- Yang, J. C., Hu, L. Q., & Wang, C. H. (2019). Population dynamics modify urban residents' exposure to extreme temperatures across the United States. *Sci. Adv.*, 5, <https://doi.org/10.1126/sciadv.aay3452> eaay3452.
- Yang, W., Luan, Y., Liu, X., Yu, X., Miao, L., & Cui, X. (2017). A new global anthropogenic heat estimation based on high-resolution nighttime light data. *Sci. Data*, 4, Article 170116. <https://doi.org/10.1038/sdata.2017.116>.
- Zhai, J., Liu, R., Liu, J., Zhao, G., & Huang, L. (2014). Radiative forcing over China due to albedo change caused by land cover change during 1990–2010. *J. Geogr. Sci.*, 24, 789–801. <https://doi.org/10.1007/s11442-014-1120-4>.
- Zhang, G., J., Cai, M., & Hu, A. (2013). Energy consumption and the unexplained winter warming over northern Asia and North America. *Nat. Clim. Change*, 3, 466–470. <https://doi.org/10.1038/NCLIMATE1803>.
- Zhang, N., Wang, X., Chen, Y., Dai, W., & Wang, X. (2016). Numerical simulations on influence of urban land cover expansion and anthropogenic heat release on urban meteorological environment in Pearl River Delta. *Theor. Appl. Climatol.*, 126, 469–479. <https://doi.org/10.1007/s00704-015-1601-0>.
- Zhang, X., & Caldeira, K. (2015). Time scales and ratios of climate forcing due to thermal versus carbon dioxide emissions from fossil fuels. *Geophys. Res. Lett.*, 42, 4548–4555. <https://doi.org/10.1002/2015GL063514>.